Probing ferroelectricity by x-ray absorption spectroscopy in molecular crystals

Fujie Tang ,[1] Xuanyuan Jiang,[2] Hsin-Yu Ko ,[3] Jianhang Xu ,[1] Mehmet Topsakal,[4,*] Guanhua Hao ,[2] Alpha T. N'Diaye,[5] Peter A. Dowben ,[2] Deyu Lu,[4] Xiaoshan Xu ,[2,†] and Xifan Wu ,[1,‡]

[1]*Department of Physics, Temple University, Philadelphia, Pennsylvania 19122, USA*
[2]*Department of Physics and Astronomy, Nebraska Center for Materials and Nanoscience, University of Nebraska,*
Lincoln, Nebraska 68588, USA
[3]*Department of Chemistry, Princeton University, Princeton, New Jersey 08544, USA*
[4]*Center for Functional Nanomaterials, Brookhaven National Laboratory, Upton, New York 11973, USA*
[5]*Advanced Light Source, Lawrence Berkeley National Laboratory, Berkeley, California 94720, USA*

We carry out x-ray absorption spectroscopy experiment at the oxygen K edge in croconic acid ($C_5H_2O_5$) crystal as a prototype of ferroelectric organic molecular solid, whose electric polarization is generated by proton transfer. The experimental spectrum is well reproduced by the electron-hole excitation theory simulations from configuration generated by *ab initio* molecular dynamics simulation. When inversion symmetry is broken in the ferroelectric state, the hydrogen bonding environment on the two bonded molecules become inequivalent. Such a difference is sensitively probed by the bound excitation in the pre-edge, which is strongly localized on the excited molecules. Our analysis shows that a satellite peak in the pre-edge will emerge at higher excitation energy, which serves as a clear signature of ferroelectricity in the material.

I. INTRODUCTION

Ferroelectricity (FE) is an important material property describing the ability of some solids to sustain a spontaneous electric polarization, whose direction can be reversed under applied electric fields [1–6]. Because of its importance in both fundamental science and technology, extensive techniques have been developed to study the nature of FE since its discovery in the late 1910s. In experiments, the polarization profile is sensitive to the optical second harmonic generation [7], and the electric dipole density in crystals can be quantitatively determined in the hysteresis measurement through the flow of the polarization current [8]. Spectroscopy experiment, such as x-ray absorption spectroscopy (XAS), is also widely applied in solids [9,10]. In the XAS process, the timescale of electron-hole excitation is much shorter than that of the lattice vibrations. Therefore, XAS spectra record the electronic structural information corresponding to its instantaneous local environment [11–16]. However, in conventional oxide ferroelectrics, XAS spectra were only employed to indirectly infer the underlying FE orderings since the degree of hybridization between transition metal and oxygen is only slightly affected by the polar distortion [17,18]. Unfortunately, an unambiguous XAS signature of FE so far remains elusive, which requires more abrupt electronic structure changes induced by broken inversion symmetry.

Recently, the successful synthesis of hydrogen- (H) bonded organic ferroelectrics has attracted much attention [19–26]. In FE molecular crystals, such as croconic acid (CA), the measured polarizations are comparable to that of $BaTiO_3$ as one of the most studied ferroelectrics [27,28]. Molecular ferroelectrics exhibit at much lower switching fields than oxide ferroelectrics [19–22]. Such intriguing physics originates from the unusual way in generating FE. For CA, the polar distortion arises from the large displacements of protons, which is conceptually described as the *proton transfer* mechanism [10,22,29]. When a proton is located at the middle point of two oxygen atoms along an H bond, the two molecules formed a symmetric H-bond environment. The polarization emerges as long as protons displace away from the high symmetry point along the H-bonding direction [30]. Besides, the protons also make significant electronic contribution to the overall polarization due to the large charge transfer accompanied by proton transfer. Such a large electronic structure changes via proton transfer in molecular crystals also provides an ideal platform where FE can be probed by XAS. In the organic ferroelectrics, the two bonded molecules no longer have the same H-bonding strength once proton transfer occurs. The resulting two distinct H-bonding configurations break the inversion symmetry and should have clear signatures in XAS spectrum. Indeed, XAS at the oxygen K edge has recently been applied as a sensitive probe for the H-bonding environment in water [11–13,15,16,31].

Here we address the above issues by combined experimental and theoretical studies of oxygen K-edge XAS in CA molecular crystal. Based on the electron-hole excitation theory [13], the computed XAS spectrum agrees well with our experimental one at room temperature. Our electronic

---

*Present address: Nuclear Science and Technology Department, Brookhaven National Laboratory, Upton, New York 11973, USA.
†Corresponding author: xiaoshan.xu@unl.edu
‡Corresponding author: xifanwu@temple.edu

structural analyses further reveal that proton transfer not only generates a large electric polarization that strongly couples to the π bonding state but also lifts the degeneracy of the excitation with π^* antibonding character represented by the pre-edge of XAS. With the development of FE via proton transfer, two equivalent H-bonded molecules evolve into H-bond donor and H-bond acceptor molecules, respectively. Influenced by the Coulomb potential of the proton, the π^* exciton on the H-bond donor molecule becomes delocalized with an increased excitation energy; and the opposite effect is observed for the π^* exciton on the H-bond acceptor molecule. Therefore, the resulting split pre-edge features at $\sim$530 and $\sim$532 eV, respectively, carry out unambiguous spectral signature of the broken inversion symmetry. Our method provides a new probe for FE via proton transfer mechanism, which is ready to be applied on other molecular ferroelectrics in general.

II. METHODS

The polycrystalline CA films (450 nm) were deposited on 10×10 mm^2 highly ordered pyrolytic graphite substrates using physical vapor deposition in high vacuum (1.0×10^{-7} Torr), with a growth rate of 0.1 Å/s. The film morphology and thickness were characterized by atomic force microscopy and the root-mean-square roughness was found to be about 16 nm [26]. The FE property of the current CA sample has been proven by the polarization hysteresis measurement reported in the previous work [26]. The XAS spectra were carried out at the bending magnet beamline 6.3.1, in the Advanced Light Source of the Lawrence Berkeley National Laboratory. The photon flux was estimated to be 1.65 photons/(s μm^2). The XAS spectra were taken at 300 K, in the total electron yield mode, within the energy range around the O K edge. Note that the Curie temperature of CA is higher than the decomposition temperature [20].

The theoretical predictions of the structure of the CA crystal were performed at both $T = 0$, 300 K based on density-functional theory (DFT) [32,33] and *ab initio* molecular dynamics (AIMD) [34,35] under isothermal-isobaric ensemble (constant NpT ensemble) [36,37] as implemented in Quantum Espresso [38]. The local-density approximations (LDA), the generalized gradient approximations (GGA) in the form of Perdew–Burke–Ernzerhof (PBE) functional, the strongly-constrained and appropriately-normed (SCAN) functional, and SCAN0 (hybrid-meta GGA, which mixed with 10% Hartree-Fock exchange) [39,40] to describe the electron exchange and correlation using a linear-scaling algorithm [41,42] based on maximally localized Wannier functions [43,44]. We used energy cut-off of 200 Ry to get the better convergence of lattice parameters with Monkhorst-Pack $4 \times 6 \times 3$ k-points sampling. All atom positions were fully relaxed until the force on each atom was less than 10^{-6} a.u.. Furthermore, we carried out the Born-Oppenheimer molecular dynamics (BOMD) simulations with NpT ensemble for LDA, PBE, and SCAN functionals with initial relaxed structures, while the Car-Parrinello molecular dynamics (CPMD) simulations with NpT (isothermal-isobaric) ensemble for the SCAN0 functional were carried out with initial relaxed structures by using Quantum Espresso. The NpT simulation is performed by using the Parrinello-Rahman barostat as implemented in the Quantum Espresso code package. The choice

for using BOMD instead of CPMD with LDA, PBE, and SCAN functionals is due to the unstable NpT simulation because of the relative underestimated band gap of LDA and semilocal functional. The simulation cell contains eight croconic acid molecules. The temperature is set at 300 K by using single Nose-Hoover chain thermostat. The time step for the equation of motion is set to 2.0 a.u. for CPMD and 20.0 a.u. for BOMD. We adopted the norm-conserving Vanderbilt pseudopotential for C, O, and H atoms and set the kinetic energy cutoff of the electronic wave function as 130 Ry. We equilibrated the system with 2 ps, which has been proved to be enough for molecular crystal. Then we performed CPMD simulation production run up to 7 ps for LDA, PBE, and SCAN functionals, while the length of trajectory for production run with SCAN0 is 5 ps. We picked up one snapshot from SCAN0 trajectory to perform XAS calculation.

The theoretical XAS spectrum was computed based on our recently developed computational method in treating electron-hole interactions [12,13,15,16]. In order to sample the different local environment of oxygen atom, we excited all of 40 oxygen atoms in the cell where the snapshot is taken from trajectory of SCAN0-AIMD. Since we are focusing on the molecular crystal, even for the room temperature, one snapshot is more than enough to converge the XAS spectra. The theoretical structure and polarization predicted by AIMD simulation at the SCAN0 level are superior compared with the ones based on commonly used semilocal functionals.

III. RESULTS AND DISCUSSIONS

The CA molecule is composed of pentagon of carbon atoms, each of which is bonded to an oxygen atom. In the condensed phase, its molecular alignment is governed by the intermolecular forces provided by the H bond. As shown in Fig. 1(a), the two molecules within the same layer are connected by the *terrace* H-bond, and the two neighboring layers are linked by the *hinge* H bond with a folding angle around 68°. In crystals, the above folding layers result in zigzag shapes extending along three crystal directions. At room temperature, the corresponding lattice constants and volume are determined respectively to be $a = 8.62(8.50)$ Å, $b = 5.10(5.18)$ Å, $c = 10.92(10.82)$ Å, and $V = 479.5(476.4)$ Å^3. In the above, the numbers outside (in) the parentheses are our experimental (theoretical) values. At $T = 300$ K, our SCAN0-AIMD simulation in croconic acid crystal yields an average electric polarization of 30.30 μC/cm^2, which is close to the experimentally measured polarization of 30 μC/cm^2 [21]. It should be stressed that the hybrid functional SCAN0 at the state-of-the-art meta-GGA level gives superior predictions of the H-bonded molecular structures than the conventional functional approximations.

The vector symbols in Fig. 1(a) denote the structural distortions in CA crystal from its hypothetical paraelectric phase to the FE ground state, with Pbcm and Pca2$_1$ space group symmetry, respectively [20,29,30,45]. Clearly, the distortions are dominated by proton transfer as evidenced by the large displacements of protons along the H-bonding directions threading oxygen atoms on two neighboring molecules. The proton transfer is accompanied by a buckling mode of the oxygen atoms that slightly twists the pentagons [30].
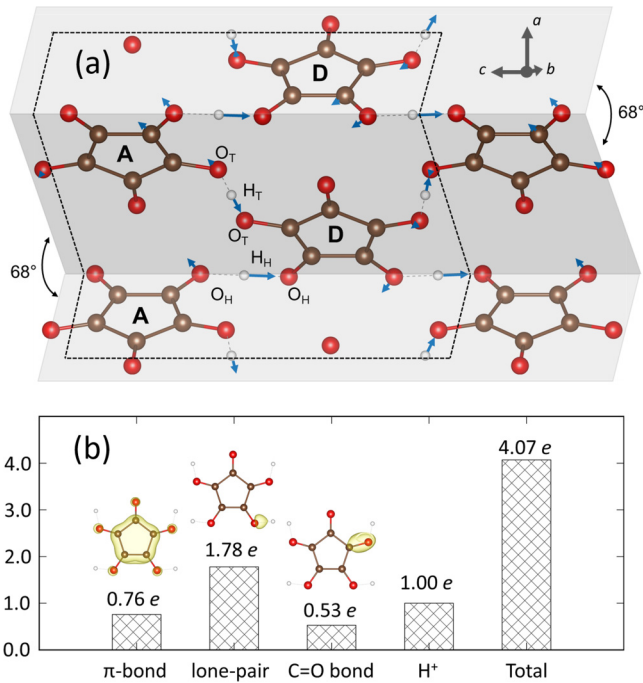
FIG. 1. (a) The schematic of the CA crystal unit cell and the vector symbols denote the structure distortion. (b) Decomposition of Born effective charge of the *hinge* H atom onto the contributions from Wannier functions of various bonding characteristics.
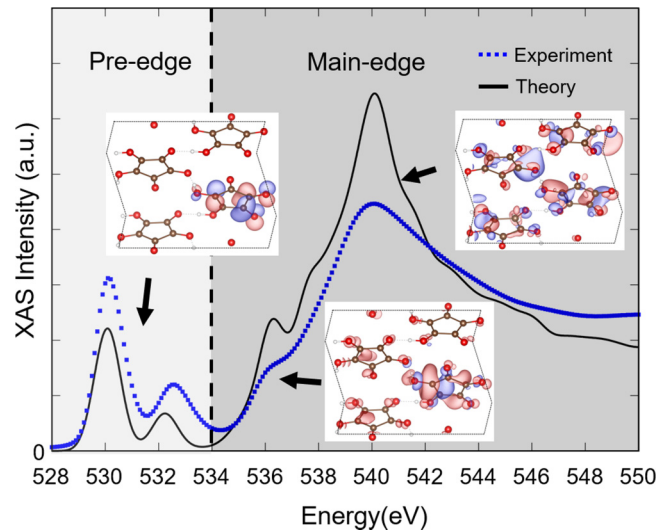

FIG. 2. The experimental (blue dashed line) and theoretical (black solid line) near edge x-ray absorption spectra of CA crystal. The theoretical XAS spectra was generated by using the configuration from *ab initio* molecular dynamics with SCAN0 at 300 K. The inserted figures are the representative orbital for pre-edge, kink, and main-edge features of XAS. The excited oxygen atom is located in the downright CA molecule.

While the protons are in the middle of the two neighboring molecules, the crystal is invariant under a reflection operation, and therefore the FE is forbidden. Once the proton moves away from the middle point, the inversion symmetry is broken, leaving one of the molecules as the H-bond donor and the other as the H-bond acceptor, as shown in Fig. 1(a). The proton transfer not only induces the polarity but also plays a key role in stabilizing the FE. For protons along either the *hinge* or the *terrace* direction, the computed dynamic effective charge tensor from linear response theory is found to have a very large diagonal element; the value for the *hinge* H atom is $Z^*_{H,PT} = 4.1e$ along the proton transfer (PT) direction [28,46,47]; whereas the other diagonal and off-diagonal elements of the effective charge tensor are relatively small. The much larger effective charge than its nominal charge is not unusual in FE materials. It indicates that FE is promoted by the charge transfer under proton transfer by favoring the long-range Coulomb interaction over the short-range repulsion [48,49]. Based on the modern theory of polarization [43,44], we further decompose $Z^*_{H,PT}$ into the contributions from centers of maximally localized Wannier functions as shown in Fig. 1(b). As expected, $Z^*_{H,PT}$ is mainly composed of the Wannier functions of the lone pair electrons, which describes the local electronic structural changes in the process of proton transfer. Surprisingly, a significant electronic contribution in $Z^*_{H,PT}$ is also originates from the Wannier functions of the π bond on the H-bonded molecules, as shown in Fig. 1(b). It suggests that the ionic displacement of the proton transfer is actually strongly coupling to the π bond. Indeed, it has long been proposed that the FE switching process largely involves the delocalized π bond in these organic FE materials [20,22].

The broken inversion symmetry should not only be reflected in the electric properties of the bonding electrons but also leave a trace on the electron-hole excitations with antibonding which could be probed by XAS. As shown in Fig. 2, we present near the edge x-ray absorption the fine structure of the CA crystal. Within the ~20 eV range, a good agreement can be seen between experiment and theory in terms of both spectral intensity and line shape. The pre-edge feature of XAS is located at relatively lower energies from 528 to 534 eV. In the pre-edge, one sharp peak can be identified centered at 530.1 eV from experiment (530.1 eV from theory), which is followed by a less-pronounced feature at a slightly higher energy of 532.6 eV (532.1 eV). Compared to the pre-edge feature, the main-edge of XAS from 534 to 548 eV is composed of broader spectral signals with stronger intensities centered around 540 eV (540 eV). Moreover, a kink feature can also be seen at 536.1 eV (536.1 eV) on the left shoulder of the main edge in XAS.

Accurate prediction of the XAS spectrum allows us to further explore the spectral signature of FE in CA. To this end, we rely on theory to study the spectral changes when the FE ordering is artificially varied in the crystal. Specifically, we start from the centrosymmetric phase with zero FE distortion $\lambda_{FE} = 0$ and then gradually increase the polarity via λ_{FE} in the structure. In the above, the $\lambda_{FE} = 1$ is normalized to the amplitude of polar mode Γ_2^-, which is extracted from fully relaxed structure of CA crystal at ground state of $T = 0$ K facilitated by group theory analysis [45]. The resulting XAS spectra for CA crystal with different magnitudes of FE distortions of $\lambda_{FE} = 0$, 0.6, and 1 are shown in Fig. 3(a). It can be seen that the main edge of XAS is rather insensitive to the presence of FE ordering. The general line shape of the main edge remains more or less unaffected when the FE
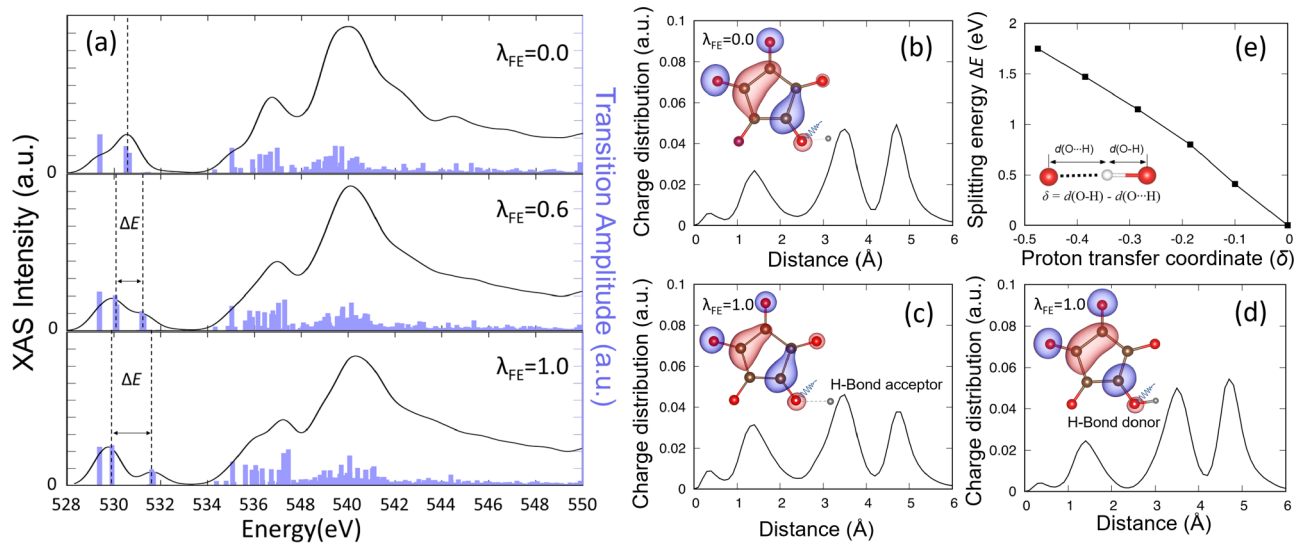
FIG. 3. (a) The calculated XAS spectra (black) and XAS transition amplitude plots (purple) for CA crystal with different magnitudes of FE distortions of $\lambda_{FE} = 0$, 0.6, and 1. The dashed lines denote the peak positions when excited oxygen atoms are in different H-bonding environment. Note that the peak at around 529.4 eV belongs to the isolated oxygen atom, whose peak position remains the same with the development of FE. [(b), (c) and (d)] Charge distribution of the excited oxygen atoms (*hinge* direction) where the excited oxygens are the oxygen atom in the paraelectric phase, the H-bond acceptor pair oxygen atom in the FE phase, and the H-bond donor pair oxygen atom in the FE phase, respectively. The zero point is located at the excited oxygen atom. The inserted figures in (b), (c), and (d) are selected excited molecular orbitals, where the white dot indicates the excited oxygen atoms. (e) The relation between splitting energy ΔE and proton transfer coordinate δ. The inserted figure is the schematic of the definition of proton transfer coordinate.

distortion is varied in the crystal. In sharp contrast, the pre-edge of XAS undergoes qualitative changes on the development of FE distortion. In the hypothetical paraelectric structure, only one broad feature is observed in the pre-edge. Once the FE distortion is added into the hypothetical paraelectric crystal structure, a second peak emerges at a slightly higher energy. With the increasing magnitude of polar distortions, the satellite peak continues moving toward higher energies until it evolves into an experimentally observed feature at 533 eV in Fig. 2 when $\lambda_{FE} = 1$. Clearly, the appearance of the satellite peak in the pre-edge signifies the development of FE in the material. In XAS spectroscopy, the oxygen $1s$ electron at the core level is excited, probing the p character in the unoccupied bands. Therefore, such a feature should be closely associated with the orbital assignment of the excitons.

We assign the pre-edge to a bound exciton which is strongly localized on the excited molecule in the crystal [50]. The exciton in pre-edge is the π^* state, which is antibonding in nature as shown in the insert of Fig. 2. The π^* characteristic can be traced back to the low-lying states of molecular excitation with similar orbital symmetry in the gas phase of CA. In the π^* orbital on the CA, p character can be identified on the excited oxygen atom, which gives rise to a strong transition amplitude that is responsible for the pre-edge feature. Moreover, in the condensed phase, the antibonding orbital will be influenced by the local H-bonding environment in a nontrivial way.

For each $C_5H_2O_5$ molecule in the crystal, four of the carbon-bonded oxygen atoms will be also H bonded to neighboring molecules through the intermolecular protons. In the centrosymmetric phase with $\lambda_{FE} = 0$, the proton is right in the middle of the two molecules. As a result, the

symmetric H-bonding environments are formed on each of the two bonded molecules. For the molecules bonded along the aforementioned *terrace* and *hinge* directions, their H-bonding strengths are rather similar because of the similar intermolecular distances around 2.41 Å. As required by the inversion symmetry, exactly the same π^* excitonic state, and therefore the same transition matrix elements, will be generated for any one of the H-bonded pair oxygen atoms being excited in the pre-edge as shown in Fig. 3(b). As a result, a sharp peak at 530.6 eV is formed in the pre-edge of XAS, which originates from the almost-degenerate XAS transition amplitudes for all the excited oxygen atoms in symmetric H-bonding environment. Besides the H-bonded oxygen atoms, there is also one nonbonded oxygen atom in each $C_5H_2O_5$ molecule. Without accepting a proton, the bare lone electron pair generates a more attractive core-hole potential when it is excited in XAS. Indeed, compared to that on the bonded oxygens, the π^* excitonic state localized on the nonbonded oxygen has a slightly lower transition energy at 529.4 eV in Fig. 3(a). Nevertheless, the feature of the pre-edge is mainly determined by H-bonded oxygen atoms in the hypothetical paraelectric phase. The pre-edge is skewed to the left due to the exciton on the nonbonded oxygen atoms.

By including FE ordering into the crystal structure with $\lambda_{FE} = 0.6$ and 1.0, the inversion symmetry is broken. As described above, FE distortion is accompanied by large proton transfer. For the two bonded molecules, proton transfer drives a proton to leave one molecule to get close to the other. Obviously, the two molecules are not in equivalent H-bonding environments any longer; instead, they become an H-bond acceptor and H-bond donor, respectively, as shown in Figs. 3(c) and 3(d). By carrying out positive electron charge,

the proton displacement in turn affects the energy and localization of the bound π^* exciton in the pre-edge. As far as the H-bond acceptor molecule is concerned, the increased distance between the oxygen and proton leaves the excited oxygen with a stronger core-hole potential which is less affected by the Coulombic attraction of the proton. Therefore, the π^* exciton is more localized on the excited oxygen in Fig. 3(c), which enhances the absorption intensity with a slightly lower transition energy. On the contrary, the opposite effect occurs on the H-bond donor molecule. The localization of bound π^* exciton, on the excited oxygen, is diminished in Fig. 3(d) due to the increased Coulombic interaction from the closer proton. Consistently, the absorption intensity is decreased and shifted to a higher transition energy as shown in Fig. 3(a). As a result, the development of FE splits the pre-edge, resulting in a satellite peak at higher excitation energy. Furthermore, the splitting energy ΔE is roughly linearly proportional to the magnitude of proton transfer as measured by the proton transfer coordinate δ in Fig. 3(e). The above is consistent with the first-order approximation of electrostatic energy changes which are perturbed by the proton transfer.

Compared to the bound exciton in the pre-edge features, the main-edge should be assigned to the exciton resonance states as shown in Fig. 2 [50]. In particular, two main orbital characteristics are identified here. The peak region around 540 eV is attributed to the exciton resonance states with antibonding σ^* character. While the kink feature is due to the transitions from exciton resonance states with π^* orbitals on the excited molecule, which are hybridized with σ^* on the surrounding molecules [50]. Because of their unbound nature, these exciton resonance states are strongly delocalized over the entire crystal. Therefore, the observed feature in the main edge is not from the large transition matrix element but due to the electronic density states in excited states. Not surprisingly, these delocalized orbitals are not sensitive to the variation of FE ordering, which applies a local change on the H-bonding environment in the vicinity of excited oxygen atoms. Indeed, the above is consistent with the fact that the general main-edge feature is barely changed in Fig. 3(d) under the artificially adjusted magnitudes of polar distortion λ_{FE} in the molecular crystal.

IV. CONCLUSION

In conclusion, we demonstrate that x-ray absorption spectroscopy can be employed as a sensitive local probe for broken spatial inversion symmetry in CA, which is a prototypical H-bonded organic molecular crystal. The emergence of a satellite feature in the pre-edge with a relatively higher transition energy can be denoted as an unambiguous signature of FE. It arises from the bound π^* exciton whose locality and energy are affected by the two inequivalent H-bonding configurations distinctly as a result of inversion symmetry breaking. A similar scenario facilitated by proton transfer lies at the heart of FE as well as the antiferroelectrics in all the H-bonded molecular crystals; therefore our approach should be generally applicable to the new series of organic ferroelectric and antiferroelectric materials.

[1] M. E. Lines and A. M. Glass, *Principles and Applications of Ferroelectrics and Related Materials* (Oxford University Press, Oxford, 2001) p. 694.

[2] M. Dawber, K. M. Rabe, and J. F. Scott, Rev. Mod. Phys. **77**, 1083 (2005).

[3] K. M. Rabe, M. Dawber, C. Lichtensteiger, C. H. Ahn, and J.-M. Triscone, *Physics of Ferroelectrics: A Modern Perspective* (Springer, Berlin, 2007), pp. 1–30.

[4] J. F. Scott, Science **315**, 954 (2007).

[5] R. Xu, S. Liu, I. Grinberg, J. Karthik, A. R. Damodaran, A. M. Rappe, and L. W. Martin, Nat. Mater. **14**, 79 (2015).

[6] S. Liu, I. Grinberg, and A. M. Rappe, Nature **534**, 360 (2016).

[7] S. A. Denev, T. T. Lummen, E. Barnes, A. Kumar, and V. Gopalan, J. Am. Ceram. Soc. **94**, 2699 (2011).

[8] H. N. Lee, H. M. Christen, M. F. Chisholm, C. M. Rouleau, and D. H. Lowndes, Nature **433**, 395 (2005).

[9] A. L. Kholkin, S. V. Kalinin, A. Roelofs, and A. Gruverman, in *Scanning Probe Microscopy: Electrical and*

Electromechanical Phenomena at the Nanoscale (Springer, 2007), pp. 173–214.

[10] K. Iwano, Y. Shimoi, T. Miyamoto, D. Hata, M. Sotome, N. Kida, S. Horiuchi, and H. Okamoto, Phys. Rev. Lett. **118**, 107404 (2017).

[11] P. Wernet, D. Nordlund, U. Bergmann, M. Cavalleri, N. Odelius, H. Ogasawara, L. Å. Näslund, T. K. Hirsch, L. Ojamäe, P. Glatzel, L. G. Pettersson, and A. Nilsson, Science **304**, 995 (2004).

[12] W. Chen, X. Wu, and R. Car, Phys. Rev. Lett. **105**, 017802 (2010).

[13] D. Prendergast and G. Galli, Phys. Rev. Lett. **96**, 215502 (2006).

[14] F. Bisti, A. Stroppa, S. Picozzi, and L. Ottaviano, J. Chem. Phys. **134**, 174505 (2011).

[15] Z. Sun, M. Chen, L. Zheng, J. Wang, B. Santra, H. Shen, L. Xu, W. Kang, M. L. Klein, and X. Wu, Phys. Rev. B **96**, 104202 (2017).

[16] Z. Sun, L. Zheng, M. Chen, M. L. Klein, F. Paesani, and X. Wu, Phys. Rev. Lett. **121**, 137401 (2018).

[17] B. Ravel and E. A. Stern, Phys. B **208-209**, 316 (1995).

[18] M. E. M. Cabrera, *Multifunctional Polycrystalline Ferroelectric Materials: Processing and Properties* (Springer Netherlands, Dordrecht, 2011), pp. 281–346.

[19] S. Horiuchi and Y. Tokura, Nat. Mater. **7**, 357 (2008).

[20] S. Horiuchi, Y. Tokunaga, G. Giovannetti, S. Picozzi, H. Itoh, R. Shimano, R. Kumai, and Y. Tokura, Nature **463**, 789 (2010).

[21] S. Horiuchi, F. Kagawa, K. Hatahara, K. Kobayashi, R. Kumai, Y. Murakami, and Y. Tokura, Nat. Commun. **3**, 1308 (2012).

[22] S. Horiuchi, K. Kobayashi, R. Kumai, and S. Ishibashi, Nat. Commun. **8**, 14426 (2017).

[23] S. Horiuchi, J. Tsutsumi, K. Kobayashi, R. Kumai, and S. Ishibashi, J. Mater. Chem. C **6**, 4714 (2018).

[24] M. Owczarek, K. A. Hujsak, D. P. Ferris, A. Prokofjevs, I. Majerz, P. A. Szklarz, H. Zhang, A. A. Sarjeant, C. L. Stern, R. Jakubas, S. Hong, V. P. Dravid, and J. F. Stoddart, Nat. Commun. **7**, 13108 (2016).

[25] A. Stroppa, D. Di Sante, S. Horiuchi, Y. Tokura, D. Vanderbilt, and S. Picozzi, Phys. Rev. B **84**, 014101 (2011).

[26] X. Jiang, H. Lu, Y. Yin, X. Zhang, X. Wang, L. Yu, Z. Ahmadi, P. S. Costa, A. D. Dichiara, X. Cheng, A. Gruverman, A. Enders, and X. Xu, Appl. Phys. Lett. **109**, 102902 (2016).

[27] R. D. King-Smith and D. Vanderbilt, Phys. Rev. B **49**, 5828 (1994).

[28] W. Zhong, R. D. King-Smith, and D. Vanderbilt, Phys. Rev. Lett. **72**, 3618 (1994).

[29] Y. Cai, S. Luo, Z. Zhu, and H. Gu, J. Chem. Phys. **139**, 044702 (2013).

[30] D. Di Sante, A. Stroppa, and S. Picozzi, Phys. Chem. Chem. Phys. **14**, 14673 (2012).

[31] J. S. Tse, D. M. Shaw, D. D. Klug, S. Patchkovskii, G. Vankó, G. Monaco, and M. Krisch, Phys. Rev. Lett. **100**, 095502 (2008).

[32] P. Hohenberg and W. Kohn, Phys. Rev. **136**, B864 (1964).

[33] W. Kohn and L. J. Sham, Phys. Rev. **140**, A1133 (1965).

[34] R. Car and M. Parrinello, Phys. Rev. Lett. **55**, 2471 (1985).

[35] D. Marx and J. Hutter, *Ab Initio Molecular Dynamics: Basic Theory and Advanced Methods* (Cambridge University Press, Cambridge, UK, 2009).

[36] M. Parrinello and A. Rahman, Phys. Rev. Lett. **45**, 1196 (1980).

[37] M. Bernasconi, G. Chiarotti, P. Focher, S. Scandolo, E. Tosatti, and M. Parrinello, J. Phys. Chem. Solids **56**, 501 (1995).

[38] P. Giannozzi, O. Andreussi, T. Brumme *et al.*, J. Phys.: Condens. Matter **29**, 465901 (2017).

[39] V. N. Staroverov, G. E. Scuseria, J. Tao, and J. P. Perdew, J. Chem. Phys. **119**, 12129 (2003).

[40] J. Sun, A. Ruzsinszky, and J. P. Perdew, Phys. Rev. Lett. **115**, 036402 (2015).

[41] X. Wu, A. Selloni, and R. Car, Phys. Rev. B **79**, 085102 (2009).

[42] R. A. DiStasio, B. Santra, Z. Li, X. Wu, and R. Car, J. Chem. Phys. **141**, 084502 (2014).

[43] N. Marzari, A. A. Mostofi, J. R. Yates, I. Souza, and D. Vanderbilt, Rev. Mod. Phys. **84**, 1419 (2012).

[44] N. Marzari and D. Vanderbilt, Phys. Rev. B **56**, 12847 (1997).

[45] E. Kroumova, M. L. Aroyo, J. M. Perez-Mato, A. Kirov, C. Capillas, S. Ivantchev, and H. Wondratschek, Phase Transit. **76**, 155 (2003).

[46] R. D. King-Smith and D. Vanderbilt, Phys. Rev. B **47**, 1651 (1993).

[47] M. Sharma, R. Resta, and R. Car, Phys. Rev. Lett. **95**, 187401 (2005).

[48] P. Ghosez, X. Gonze, and J. P. Michenaud, Europhys. Lett. **33**, 713 (1996).

[49] G. A. Samara, T. Sakudo, and K. Yoshimitsu, Phys. Rev. Lett. **35**, 1767 (1975).

[50] G. Hähner, Chem. Soc. Rev. **35**, 1244 (2006).